INTERNATIONAL JOURNAL FOR NUMERICAL METHODS IN FLUIDS
Int. J. Numer. Meth. Fluids 2007; **54**:47–72
Published online 21 November 2006 in Wiley InterScience (www.interscience.wiley.com). DOI: 10.1002/fld.1392

Euler solutions using flux-based wave decomposition

Nash'at Ahmad[1,*,†] and John Lindeman[2]

[1]*Science Applications International Corporation, McLean, VA 22102, U.S.A.*
[2]*George Mason University, Fairfax, VA 22030, U.S.A.*

SUMMARY

The Euler equations are solved for non-hydrostatic atmospheric flow problems in two dimensions using a high-resolution Godunov-type scheme. The Riemann problem is solved using a flux-based wave decomposition suggested by LeVeque. This paper describes in detail, the design and implementation of the Riemann solver used for computing the Godunov fluxes. The methodology is then validated against benchmark cases for non-hydrostatic atmospheric flows. Comparisons are made with solutions obtained from the National Center for Atmospheric Research's state-of-the-art numerical model. The method shows promise in simulating non-hydrostatic flows, which are characterized by steep gradients on the meso-, micro- and urban-scales. Copyright © 2006 John Wiley & Sons, Ltd.

Received 20 June 2006; Revised 25 September 2006; Accepted 30 September 2006

KEY WORDS: atmospheric flows; Godunov method; flux-based wave decomposition

1. INTRODUCTION

Godunov-type methods [1, 2] have gained wide popularity in the scientific computing community for solving the systems of hyperbolic conservation laws. Godunov's unique approach to numerical modelling of fluid flow is characterized by introducing physical reasoning in the development of the numerical scheme [3]. The construction of the scheme itself is based upon the physical phenomenon described by the equation sets. These finite volume discretizations are conservative and have the ability to resolve regions of steep gradients accurately, thus avoiding dispersion errors in the solution. Positivity of scalars (an important factor when considering the transport of micro-physical quantities) is also guaranteed by applying the *total variation diminishing* (TVD) condition appropriately.

*Correspondence to: Nash'at Ahmad, Science Applications International Corporation, 1710 SAIC Drive, M/S 2-3-1, McLean, VA 22102, U.S.A.
†E-mail: ahmadn@saic.com

In recent years, there has been a growing interest in using Godunov-type methods for atmospheric flow problems. Ahmad *et al.* [4] have implemented a Godunov-type scheme with the Harten-Lax–van Leer-contact (HLLC) approximate Riemann solver [5] for the Euler as well as Navier–Stokes equations on unstructured adaptive grids. Botta *et al.* [6] have simulated gravity waves forming over mountains. Carpenter *et al.* [7] have applied the method for atmospheric flows using an exact Riemann solver in conjunction with the piecewise parabolic method (PPM) [8]. Carpenter *et al.* [7] show the inherent strengths of Godunov-type methods by providing a comparison with the multi-dimensional positive definite advection transport algorithm (MPDATA) [9] and the Leapfrog scheme. The important role Godunov-type methods can play in accurately resolving atmospheric phenomena characterized by steep gradients is also pointed out.

Hurricanes, tornadoes, fronts, drylines, micro-bursts and inversions are some examples of atmospheric processes, which have strong gradients of velocities, temperature and potential temperature. Fronts, for example, have large horizontal temperature and wind gradients and vertical wind shear. Strong convection in supercell thunderstorms can produce tornadoes, winds up to $\sim 50\,\mathrm{ms}^{-1}$, lightning and flash floods [10]. Drylines [11] are characterized by a strong moisture gradient in the planetary boundary layer (e.g. in the Great Plains this gradient can be up to several degrees Celsius which is much larger than the climatological average of $0.04^{\circ}\mathrm{C\,km}^{-1}$ in the dewpoint temperature). Drylines can trigger strong convective activity and winds in excess of 50 miles per hour have been observed [11]. In tornadoes (F5 category), winds between 125 and $140\,\mathrm{ms}^{-1}$ have been observed. Hurricanes are yet another example of an atmospheric process which is characterized by extreme gradients of velocities and potential temperature [12].

Traditionally, the centred finite difference schemes such as the Leapfrog scheme have been favoured for discretizing the atmospheric flow equation set. These types of schemes exhibit dispersion errors (non-physical spurious oscillations), which can contaminate the numerical results [7]. At smaller spatial and temporal scales (e.g. non-hydrostatic meso-scale flows), large gradients of velocities and other physical quantities can develop, which create stability problems for centred schemes. The application of the Leapfrog scheme on smaller scales also requires explicit time filtering for stability. The Asselin time filter, which is often used, degrades the accuracy of the scheme in time [13, 14]. Furthermore, the scheme can introduce false negatives in important scalar micro-physical quantities. To avoid false negatives, either positive definite schemes [9, 15] or flux corrected transport (FCT)-type schemes [16, 17] are often used to advect scalar quantities, while the flow solver uses centred finite differences. The upwind-biased finite difference flow solvers, which have been implemented in atmospheric models, normally do not enforce the TVD condition [18]. The one notable exception is the MPDATA scheme [9, 19–21], which is sign preserving in its basic form and can be made TVD by the appropriate use of limiters.

In this study, a Godunov-type scheme suggested by LeVeque for hyperbolic conservation laws with spatially varying flux functions [22, 23] is adapted for atmospheric flow problems. The scheme employs flux-based wave decompositions (*f-waves*) for the solution of Riemann problem and does not require the explicit definition of the Roe matrix [24] to enforce conservation. This is an important property in the context of atmospheric flows since the Roe matrix for hyperbolic conservation laws governing atmospheric flows is not readily available. The other important feature of the scheme is its ability to incorporate source term due to gravity without introducing discretization errors. Again, in the context of atmospheric flows, this is an important advantage. In the following sections, the development of the Riemann solver and its implementation within the Conservation Laws Package (CLAWPACK) is described in detail. The numerical scheme is evaluated against benchmark test cases and a comparison is made with the results obtained from the National Center

DOI: 10.1002/fld

for Atmospheric Research's state-of-the-art numerical model (the Weather Research and Forecast model—also known as the ARW-WRF model).

2. GOVERNING EQUATIONS

The basic equations governing atmospheric flows comprise a set of partial differential equations for the conservation of mass, the conservation of momentum, the conservation of energy and an equation of state to close the system. The 2D Navier–Stokes equations governing atmospheric flows are written in the conservative form (e.g. see [18, 19, 25, 26]) as

$$\frac{\partial U}{\partial t} + \frac{\partial F}{\partial x} + \frac{\partial G}{\partial y} = Q + D \tag{1}$$

where,

$$U = \begin{bmatrix} \rho \\ \rho u \\ \rho v \\ \rho\theta \end{bmatrix}, \quad F = \begin{bmatrix} \rho u \\ \rho u^2 + p \\ \rho uv \\ u\rho\theta \end{bmatrix}, \quad G = \begin{bmatrix} \rho v \\ \rho uv \\ \rho v^2 + p \\ v\rho\theta \end{bmatrix} \tag{2}$$

In the above relations, ρ is the density of fluid, u is the velocity component in the x-direction, v is the velocity component in the y-direction and p is the pressure. If a parcel of air at temperature T and pressure p is subjected to an adiabatic compression or expansion to a final reference base-state pressure ($p_0 = 10^5$ Pa), then its potential temperature, θ, is given by

$$\theta = T\left(\frac{p_0}{p}\right)^{R_d/c_p} \tag{3}$$

The system is closed by an equation of state for pressure

$$p = C_0(\rho\theta)^\gamma \tag{4}$$

where C_0 is a constant given by

$$C_0 = \frac{R_d^\gamma}{p_0^{R_d/C_v}} \tag{5}$$

In the above relations, $\gamma(= C_p/C_v = 1.4)$ is the ratio of specific heats, $R_d(= 287\,\mathrm{J\,K^{-1}\,kg^{-1}})$ is the gas constant for dry air, p_0 is the base state pressure ($= 10^5$ Pa). $C_p(= 1004\,\mathrm{J\,K^{-1}\,kg^{-1}})$ and $C_v(= 717\,\mathrm{J\,K^{-1}\,kg^{-1}})$ are the specific heats of air at constant pressure and volume, respectively. In Equation (1), Q is the source term and D is the diffusive flux term. The source term can be complex for atmospheric processes, and apart from body forces, may include terms for the heat sinks and sources produced due to the diurnal cycle of Earth, as well as micro-physical processes of cloud formations and dissipations. For the purpose of this study, a simplified source term will be used. Atmosphere is assumed to be dry and the only source term is the gravitational force acting in the vertical direction. Diffusion processes are also ignored and only the Euler solutions are considered.

DOI: 10.1002/fld

3. NUMERICAL SCHEME

The Riemann solver presented in this paper has been implemented within the CLAWPACK software. CLAWPACK is a general purpose and open-source software developed at the University of Washington, Seattle, by LeVeque [22]. The software implements high-resolution Godunov-type methods, which are explained in detail by LeVeque [22, 27–29]. The user has to provide the Riemann solver for the particular hyperbolic partial differential equation (there are several examples of Riemann solvers in the standard source distribution of CLAWPACK). The user also needs to provide the routines for model initialization and the addition of source terms, if any. The subroutines for dimensional-splitting, extensions for second-order accuracy and various limiter functions, etc. are provided in CLAWPACK. The user can also provide additional code for boundary conditions and add new limiter functions. In general, the software can be used to solve any hyperbolic partial differential equation set as long as its complete eigenstructure is known and the user provides the appropriate Riemann solver for it. Versions of CLAWPACK based on message passing interface (MPI) for distributed computing and adaptive mesh refinement (AMR) for computational efficiency, are also freely available.

In this section, a brief description of the base-line methodology implemented in CLAWPACK is given and the Riemann solver designed for the atmospheric flow equations is described in detail. The solution of the Riemann problem across each interface of a cell is a one-dimensional problem. Therefore, the basic algorithm is first described in one-dimension. The Euler equations (1)–(2) in one dimension can be written in the discrete form as

$$U_i^{n+1} = U_i^n - \Delta t \left[\frac{1}{\Delta x} (F_{i+1/2} - F_{i-1/2}) \right] \tag{6}$$

where U is the vector of conserved quantities, F is the vector of intercell fluxes calculated at the control surface of each control volume using either an exact or approximate Riemann solver. Δt and Δx are the time step and mesh resolution in x-direction, respectively. In Godunov-type solvers, the jump in U at cell centres is usually decomposed as a linear combination of the eigenvectors, $r^p_{i-1/2}$ to obtain the waves, $W^p_{i-1/2}$:

$$U_i - U_{i-1} = \sum_{p=1}^{m} \alpha^p_{i-1/2} r^p_{i-1/2} \equiv \sum_{p=1}^{m} W^p_{i-1/2} \tag{7}$$

The coefficients, $\alpha^p_{i-1/2}$, in Equation (7) are given by

$$\alpha^p_{i-1/2} = R^{-1}_{i-1/2} (U_i - U_{i-1}) \tag{8}$$

where $R_{i-1/2}$ is the matrix of right eigenvectors. The conservation is enforced by the following condition:

$$A_{i-1/2}(U_i - U_{i-1}) = F(U_i) - F_{i-1}(U_{i-1}) \tag{9}$$

where, $A_{i-1/2}$ is the Roe-averaged Jacobian [24]. Instead of solving the Riemann problem using the decomposition in Equation (7), LeVeque [22] and Bale *et al.* [23] suggest using a flux-based wave decomposition, in which the flux differences $F_i(U_i) - F_{i-1}(U_{i-1})$ are written directly as a

DOI: 10.1002/fld

linear combination of the right eigenvectors $r^p_{i-1/2}$:

$$F_i(U_i) - F_{i-1}(U_{i-1}) = \sum_{p=1}^{m} \beta^p_{i-1/2} r^p_{i-1/2} \equiv \sum_{p=1}^{m} Z^p_{i-1/2} \tag{10}$$

and

$$\beta_{i-1/2} = R^{-1}_{i-1/2}(F_i(U_i) - F_{i-1}(U_{i-1})) \tag{11}$$

The vectors $Z^p = \beta^p r^p$ are called f-waves and contain flux increments rather than increments in U. In the presence of a source term, $\psi = \rho g$, the algorithm can be extended by first setting the source term values $\psi_{i-1/2}$ at the control surfaces and then defining the f-waves $Z^p_{i-1/2}$ as follows:

$$F_i(U_i) - F_{i-1}(U_{i-1}) - \Delta x \psi_{i-1/2} = \sum_{p=1}^{m} \beta^p_{i-1/2} r^p_{i-1/2} \equiv \sum_{p=1}^{m} Z^p_{i-1/2} \tag{12}$$

$$\beta_{i-1/2} = R^{-1}_{i-1/2}(F_i(U_i) - F_{i-1}(U_{i-1}) - \Delta x \psi_{i-1/2}) \tag{13}$$

The correction for source term due to gravity in Equations (12)–(13) is applied only at the interior edges/faces. Equation (6) can now be re-written as

$$U^{n+1}_i = U^n_i - \frac{\Delta t}{\Delta x}[\mathrm{H}^+ \Delta U_{i-1/2} + \mathrm{H}^- \Delta U_{i+1/2}] \tag{14}$$

where

$$\mathrm{H}^- \Delta U_{i-1/2} = \sum_p Z^p_{i-1/2} \quad \text{if } s^p_{i-1/2} < 0 \tag{15}$$

and

$$\mathrm{H}^+ \Delta U_{i-1/2} = \sum_p Z^p_{i-1/2} \quad \text{if } s^p_{i-1/2} > 0 \tag{16}$$

$\mathrm{H}^- \Delta U_{i-1/2}$ and $\mathrm{H}^+ \Delta U_{i-1/2}$ are the fluctuations which contribute to the cell-averaged quantity U_i due to the wave propagation across the cell interfaces. In the above relations, $s^p_{i-1/2}$ are the wave speeds given by the eigenvalues of the hyperbolic equation set. Higher-order accuracy in space can be achieved by adding a correction term [22, 29]:

$$U^{n+1}_i = U^n_i - \frac{\Delta t}{\Delta x}[\mathrm{H}^+ \Delta U_{i-1/2} + \mathrm{H}^- \Delta U_{i+1/2}] - \frac{\Delta t}{\Delta x}[\tilde{F}_{i+1/2} - \tilde{F}_{i-1/2}] \tag{17}$$

where

$$\tilde{F}_{i-1/2} = \frac{1}{2} \sum_{p=1}^{m} \mathrm{sgn}(s^p_{i-1/2}) \left[1 - \frac{\Delta t}{\Delta x} |s^p_{i-1/2}| \right] \tilde{Z}_{i-1/2} \tag{18}$$

and, $\tilde{Z}^p$ is the limited value of Z^p. Bale *et al.* [23] have shown the above algorithm to be second-order accurate in space and time. The details on the implementation of wave limiters can be found in LeVeque [22, 29]. Apart from the advantages of using Godunov-type schemes, mentioned earlier (conservation, ability to simulate regions of sharp gradients, etc.), the other important features of

DOI: 10.1002/fld

LeVeque's algorithm in the context of atmospheric flows are:

- The ease with which source term due to gravity can be included without introducing discretization errors.
- The method is attractive since the Roe matrix for the system of equations in Equations (1)–(5) is not readily available.

In recent years, there has been a growing interest in developing multi-dimensional Riemann solvers (e.g. see [30]). This research, however, is still in its infancy and most Godunov-type codes for multi-dimensional problems are based on the solution of the one-dimensional Riemann problem across each cell interface. It has been shown [27, 28, 31] that the multi-dimensional information can be included into the solution even though the calculation of the Riemann problem is only one dimensional. The simplest way to extend the algorithm for multi-dimensional problems is by the dimensional-splitting technique, in which individual sweeps are performed in each spatial direction in succession. A better algorithm [27] takes into account contributions of wave fluctuations in the transverse direction.

3.1. Eigenvalues and right eigenvectors of the Euler equations governing atmospheric flows

In the Riemann solution suggested by LeVeque, it is assumed that the right eigenvectors and eigenvalues of the conservation laws can be obtained from an approximate Jacobian matrix. The eigenspace for the system of hyperbolic equations governing atmospheric flows in two dimensions is given in this section. Consider the homogeneous part of Equations (1)–(2), then the Jacobian $A(U)$ corresponding to $F(U)$ in Equation (1) can be written as

$$A(U)=\begin{bmatrix} \dfrac{\partial f_1}{\partial u_1} & \dfrac{\partial f_1}{\partial u_2} & \dfrac{\partial f_1}{\partial u_3} & \dfrac{\partial f_1}{\partial u_4} \\ \dfrac{\partial f_2}{\partial u_1} & \dfrac{\partial f_2}{\partial u_2} & \dfrac{\partial f_2}{\partial u_3} & \dfrac{\partial f_2}{\partial u_4} \\ \dfrac{\partial f_3}{\partial u_1} & \dfrac{\partial f_3}{\partial u_2} & \dfrac{\partial f_3}{\partial u_3} & \dfrac{\partial f_3}{\partial u_4} \\ \dfrac{\partial f_4}{\partial u_1} & \dfrac{\partial f_4}{\partial u_2} & \dfrac{\partial f_4}{\partial u_3} & \dfrac{\partial f_4}{\partial u_4} \end{bmatrix} = \begin{bmatrix} 0 & 1 & 0 & 0 \\ -u^2 & 2u & 0 & a^2/\theta \\ -uv & v & u & 0 \\ -u\theta & \theta & 0 & u \end{bmatrix} \tag{19}$$

where

$$U=\begin{bmatrix} u_1 \\ u_2 \\ u_3 \\ u_4 \end{bmatrix} = \begin{bmatrix} \rho \\ \rho u \\ \rho v \\ \rho\theta \end{bmatrix} \quad \text{and} \quad F(U)=\begin{bmatrix} f_1 \\ f_2 \\ f_3 \\ f_4 \end{bmatrix} = \begin{bmatrix} u_2 \\ \dfrac{u_2^2}{u_1}+C_0u_4^{\gamma} \\ \dfrac{u_2u_3}{u_1} \\ \dfrac{u_2u_4}{u_1} \end{bmatrix} \tag{20}$$

DOI: 10.1002/fld

The eigenvalues of the matrix $A(U)$ in Equation (19) are u, u, $u+a$ and $u-a$, where a is the speed of sound. The right eigenvectors of the matrix are as follows:

$$u-a:\begin{bmatrix}1\\ u-a\\ v\\ \theta\end{bmatrix},\quad u:\begin{bmatrix}0\\ 0\\ 1\\ 0\end{bmatrix},\quad u:\begin{bmatrix}1\\ u\\ 0\\ 0\end{bmatrix},\quad u+a:\begin{bmatrix}1\\ u+a\\ v\\ \theta\end{bmatrix} \tag{21}$$

Similarly, the Jacobian, $A(U)$ corresponding to $G(U)$ in Equation (1) is given by

$$A(U)=\begin{bmatrix}0 & 1 & 0 & 0\\ -uv & u & v & 0\\ -v^2 & 2v & 0 & a^2/\theta\\ -v\theta & \theta & 0 & v\end{bmatrix} \tag{22}$$

The eigenvalues and the corresponding right eigenvectors of the Jacobian in Equation (22) are

$$v-a:\begin{bmatrix}1\\ u\\ v-a\\ \theta\end{bmatrix},\quad v:\begin{bmatrix}0\\ 1\\ 0\\ 0\end{bmatrix},\quad v:\begin{bmatrix}1\\ 0\\ v\\ 0\end{bmatrix},\quad v+a:\begin{bmatrix}1\\ u\\ v+a\\ \theta\end{bmatrix} \tag{23}$$

3.2. The Riemann solver in the normal direction

Consider the matrix of right eigenvectors R (each column is a right eigenvector), for $A(U)$ corresponding to $F(U)$ in Equation (19), then the matrix R and its inverse R^{-1} (the inverse matrix R^{-1} is the matrix of left eigenvectors in which each row is a left eigenvector) can be written as

$$R=\begin{bmatrix}1 & 0 & 1 & 1\\ u-a & 0 & u & u+a\\ v & 1 & 0 & v\\ \theta & 0 & 0 & \theta\end{bmatrix},\quad R^{-1}=\begin{bmatrix}\dfrac{u}{2a} & -\dfrac{1}{2a} & 0 & \dfrac{1}{2\theta}\\ 0 & 0 & 1 & -\dfrac{v}{\theta}\\ 1 & 0 & 0 & -\dfrac{1}{\theta}\\ -\dfrac{u}{2a} & \dfrac{1}{2a} & 0 & \dfrac{1}{2\theta}\end{bmatrix} \tag{24}$$

DOI: 10.1002/fld

The β_i coefficients can now be calculated using Equation (11) by simply multiplying the inverse of the matrix of right eigenvectors with the vector containing the jumps in fluxes:

$$\begin{bmatrix}\beta_1\\ \beta_2\\ \beta_3\\ \beta_4\end{bmatrix} = \begin{bmatrix} \frac{1}{2}\left(\frac{u}{a}\Delta F_1 - \frac{1}{a}\Delta F_2 + \frac{1}{\theta}\Delta F_4\right)\\ \Delta F_3 - \frac{v}{\theta}\Delta F_4\\ \Delta F_1 - \frac{1}{\theta}\Delta F_4\\ \frac{1}{2}\left(-\frac{u}{a}\Delta F_1 + \frac{1}{a}\Delta F_2 + \frac{1}{\theta}\Delta F_4\right)\end{bmatrix} \tag{25}$$

where the jumps, ΔF_i, in the flux functions are given by

$$\begin{bmatrix}\Delta F_1\\ \Delta F_2\\ \Delta F_3\\ \Delta F_4\end{bmatrix} = \begin{bmatrix} (\rho u^j)_i - (\rho u^j)_{i-1}\\ (\rho u^j u^j)_i + p_i - (\rho u^j u^j) - p_{i-1}\\ (\rho u^j v^j)_i - (\rho u^j v^j)_{i-1}\\ (\rho\theta u^j)_i - (\rho\theta u^j)_{i-1}\end{bmatrix} \tag{26}$$

The superscript j in Equation (26) implies the component of the momentum equation (in x- or y-direction) and the subscript i denotes the cell number. The source term due to gravity is added when the Riemann problem is solved for the sweep in the y-direction:

$$\Delta F_2 = \Delta F_2 + 0.5\Delta y g[\rho^r_{i-1} + \rho^l_i] \tag{27}$$

where g is the acceleration due to gravity. The pressure in Equation (26) is calculated using the equation of state given by Equations (4)–(5). Once the β_i coefficients have been calculated, the *f-waves*, $Z^{\mathrm{p}} = \beta^{\mathrm{p}} r^{\mathrm{p}}$ can be computed as follows:

$$u-a: \begin{bmatrix}Z^1_1\\ Z^1_2\\ Z^1_3\\ Z^1_4\end{bmatrix} = \begin{bmatrix}\beta_1\\ \beta_1(u-a)\\ \beta_1 v\\ \beta_1\theta\end{bmatrix}, \quad u: \begin{bmatrix}Z^2_1\\ Z^2_2\\ Z^2_3\\ Z^2_4\end{bmatrix} = \begin{bmatrix}0\\ 0\\ \beta_2\\ 0\end{bmatrix}, \quad u: \begin{bmatrix}Z^3_1\\ Z^3_2\\ Z^3_3\\ Z^3_4\end{bmatrix} = \begin{bmatrix}\beta_3\\ \beta_3 u\\ 0\\ 0\end{bmatrix}$$

$$u+a: \begin{bmatrix}Z^4_1\\ Z^4_2\\ Z^4_3\\ Z^4_4\end{bmatrix} = \begin{bmatrix}\beta_4\\ \beta_4(u+a)\\ \beta_4 v\\ \beta_4\theta\end{bmatrix} \tag{28}$$

DOI: 10.1002/fld

Given the *f-waves* and the wave speeds $(u-a, u, u, u+a)$, the flux differences can be computed by summing up the left and right going waves across a cell interface using Equations (15)–(16). In the above relations, the sweep in x-direction is implied. Computations in the y-direction would require interchanging u and v momentums. The quantities on cell faces are calculated by taking the average of cell-centred quantities on the either side of the face.

3.3. The Riemann solver in the transverse direction

The solution of Riemann problem in the transverse direction is analogous to the solution in the normal direction. The β_i coefficients are calculated by replacing in Equation (25) the jumps in flux functions, ΔF_i by the fluctuations $\mathrm{H}^-\Delta U_{i-1/2}$ and $\mathrm{H}^+\Delta U_{i-1/2}$. The waves can now be computed as follows:

$$v-a:\begin{bmatrix} Z_1^1 \\ Z_2^1 \\ Z_3^1 \\ Z_4^1 \end{bmatrix} = \begin{bmatrix} \beta_1 \\ \beta_1 u \\ \beta_1(v-a) \\ \beta_1\theta \end{bmatrix}, \quad v:\begin{bmatrix} Z_1^2+Z_1^3 \\ Z_2^2+Z_2^3 \\ Z_3^2+Z_3^3 \\ Z_4^2+Z_4^3 \end{bmatrix} = \begin{bmatrix} \beta_3 \\ \beta_2 \\ \beta_3 v \\ 0 \end{bmatrix}$$

$$v+a:\begin{bmatrix} Z_1^4 \\ Z_2^4 \\ Z_3^4 \\ Z_4^4 \end{bmatrix} = \begin{bmatrix} \beta_4 \\ \beta_4 u \\ \beta_4(v+a) \\ \beta_4\theta \end{bmatrix} \tag{29}$$

where all waves at speed v have been summed up, since only the fluctuations are required. In all of the computations presented below, the Riemann problem in both the normal and the transverse directions was solved. The solution of the Riemann problem in the transverse direction allows larger time steps and a CFL of 0.9 was used for all simulations. It also increases the accuracy of the solution by taking into account the contributions of each wave in the transverse direction. The use of the terms 'normal direction' and 'transverse direction' is with respect to the control surfaces.

3.4. Extension of the solver to the third spatial dimension

The Riemann solver presented here can be extended to the third spatial dimension, if the wave structure is known for the equation set in three dimensions. The complete eigenspace of the hyperbolic partial differential equations governing atmospheric flows in three dimensions is given in Appendix A. The implementation of the algorithm in three dimension, using dimensional splitting would be straightforward (in each step a sweep of calculations is performed in the x-direction and then a similar sweep in y-direction is applied). However, if the corrections in the transverse direction are taken into account, then the implementation may become involved and/or computationally expensive. LeVeque [29] notes, that for some three-dimensional problems, using dimensional splitting may be more efficient computationally.

DOI: 10.1002/fld

4. RESULTS

In this section, the proposed scheme is evaluated against different benchmark cases. In the absence of closed-form solutions for Equations (1)–(5), the dynamical cores of atmospheric flow models are usually evaluated in qualitative terms. A series of test cases have been developed over the years, and the results of four of these tests are presented below—the propagation of inertia–gravity waves on non-hydrostatic scales, the convection of a warm bubble in neutral atmosphere and two variations of non-linear density currents. To better gauge the performance of the Godunov-type scheme, the results of the first two test cases are compared with the solutions obtained from the National Center for Atmospheric Research's state-of-the art WRF model.

4.1. Non-hydrostatic inertia-gravity waves

The Skamarock–Klemp [32] test for simulating inertia–gravity waves on the non-hydrostatic scale is described in this section. The domain was bounded within [0:300.0 km] × [0:10.0 km]. The model was tested for different mesh resolutions—varying from 1 km to 500 m in the horizontal and 100 to 50 m in the vertical. Periodic boundary conditions were used in the lateral and the top and bottom boundaries were set to solid walls. The domain was initialized by a constant Brunt–Väisälä frequency $N = 10^{-2}\ \mathrm{s}^{-1}$. The waves were excited by an initial potential temperature perturbation given by

$$\theta(x, y, 0) = \Delta\theta_0 \frac{\sin(\pi y/H)}{1 + (x - x_c)^2/a^2} \tag{30}$$

The amplitude of the initial potential temperature perturbation, $\Delta\theta_0$ was set to 10^{-2} K. The height H of the domain was 10 km, the perturbation half width was $a = 5$ km. The perturbation was initialized at $x_c = x_{\max}/3$, where, $x_{\max}$ is the width of the domain (300 km). A uniform u-velocity of 20 m/s was imposed in the domain and the v-velocity was set to zero. The model was run for time = 3000 s.

The ARW-WRF (version 2.1.2) model [18] was used to run the non-hydrostatic inertia gravity wave case for comparison with the proposed Godunov-type scheme. The WRF simulations were run using different orders of advection. The first simulation employed a second-order centred finite difference scheme in the horizontal and vertical, while the second simulation had fifth-order horizontal and third-order vertical advection (generally recommended by the developers of WRF). Note that the upwind-biased schemes in the WRF model do not enforce the TVD condition and, therefore, are susceptible to spurious oscillations. The solution is integrated in time using an explicit multi-stage Runge–Kutta time-marching scheme [33, 34]. In the WRF runs, the Coriolis parameter was set to zero. WRF's lower boundary was set to free-slip, and the upper boundary employed a vertical velocity = 0 at a constant pressure level. Periodic boundary conditions were set in the lateral. Horizontal grid spacing was 1000 m, and the vertical grid spacing was set such that the interval was roughly 100 m for the baseline case. The mesh resolution in the vertical was adjusted accordingly for the high-resolution run. The turbulent diffusion was turned off, and no wave-absorbing sponge layer was used in the upper part of the computational domain.

The potential temperature perturbation field and the vertical velocity for the Godunov-type scheme, after 3000 s into the simulation are shown in Figures 1 and 2, respectively. The mesh resolution in this simulation was set to 500 m in the horizontal and 50 m in the vertical. Note that the simulation results are slightly different from the analytical solution given in Skamarock and Klemp

DOI: 10.1002/fld

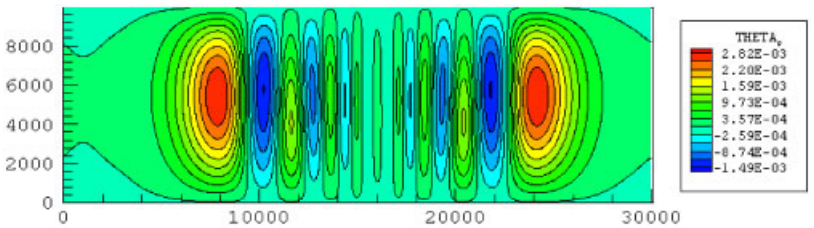

Figure 1. Non-hydrostatic inertia–gravity waves. Potential temperature perturbation (K) field after 3000 s into the simulation. Note that the x-axis has been scaled by a factor of 10 for plotting purposes. The actual domain bounds in x-direction are 0:300 km. $\Delta x = 500$ m and $\Delta y = 50$ m. Godunov solution.

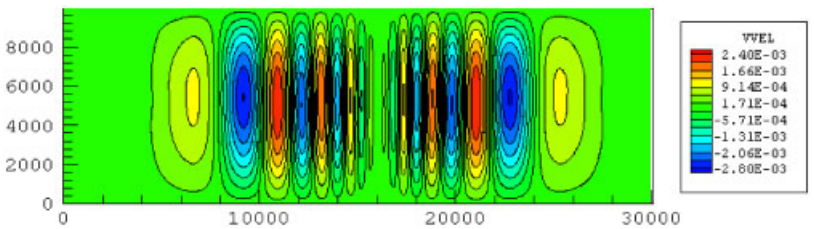

Figure 2. Non-hydrostatic inertia–gravity waves. v-velocity (m/s) field after 3000 s into the simulation. Note that the x-axis has been scaled by a factor of 10 for plotting purposes. The actual domain bounds in x-direction are 0:300 km. $\Delta x = 500$ m and $\Delta y = 50$ m. Godunov solution.

[32]. This is because the analytical solution in Skamarock and Klemp [32] assumes a Boussinesq atmosphere and the computed results presented here are obtained from a fully compressible flow model. However, the results compare well with the solutions from the WRF model which also computes the fully compressible equation set given by Equations (1)–(5). Figures 3 and 4 show the comparison of the proposed Godunov-type scheme with the WRF second-order centred and the fifth-order upwind-biased schemes at time = 3000 s. The solution obtained from the WRF fifth-order scheme is considered as the reference solution and is given by the solid line in Figures 3 and 4—the mesh resolution for the fifth-order WRF reference solution was 1 km in the horizontal and 100 m in the vertical. The high-resolution Godunov-type scheme compares well with the reference solution as well as the WRF second-order scheme. Some numerical diffusion is present in the low-resolution run but that is overcome by increasing the mesh resolution. Furthermore, it does not exhibit dispersion and phase errors apparent in the WRF second-order solution. For the Godunov-type scheme, it should be noted that if the vertical mesh resolution is too coarse (approximately >200 m), then errors start to accumulate at the lower and upper domain boundaries due to source term balancing. Since, the proposed scheme is meant for flows on high-resolution meshes (where centred finite difference schemes can break down), this would not be an issue of concern. It may be possible to avoid these errors by using a stretched grid (the vertical mesh resolution in the surface layer is typically ~ 20 m for stretched grids) near both upper and lower domain boundaries, but that needs to be tested.

DOI: 10.1002/fld

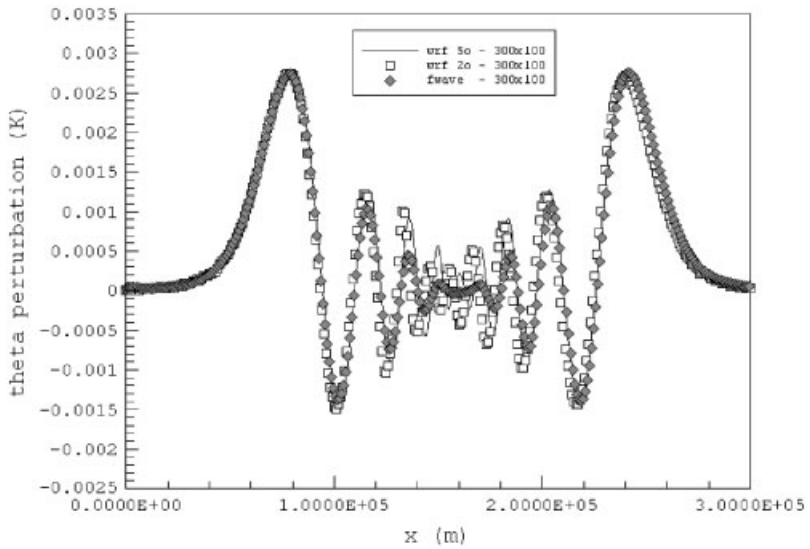

Figure 3. Non-hydrostatic inertia–gravity waves. Comparison of the Godunov-type scheme with the fifth-order and second-order WRF schemes. Theta perturbation (K) values between $x = 0$ and 300 km, for $y = 5$ km. 300×100 ($\Delta x = 1000$ m and $\Delta y = 100$ m) in the legend refer to number of cells in x- and y-direction, respectively.

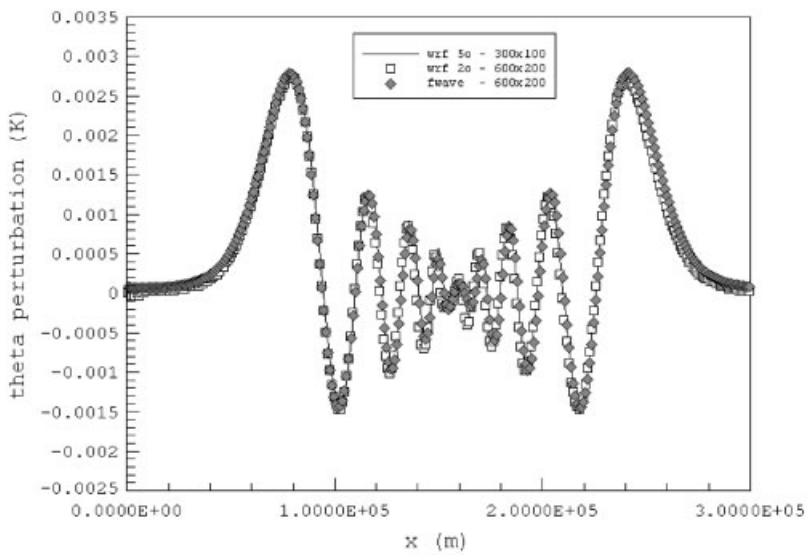

Figure 4. Non-hydrostatic inertia–gravity waves. Comparison of the Godunov-type scheme with the fifth-order and second-order WRF schemes. Theta perturbation (K) values between $x = 0$ and 300 km, for $y = 5$ km. 600×200 ($\Delta x = 500$ m and $\Delta y = 50$ m) and 300×100 ($\Delta x = 1000$ m and $\Delta y = 100$ m) in the legend refer to number of cells in x- and y-direction, respectively.

DOI: 10.1002/fld

4.2. *Convection in neutral atmosphere*

The convection in neutral atmosphere is a popular test case for validating numerical schemes for atmospheric flow simulations (e.g. [4, 7, 26, 34, 35]). In the absence of an analytical solution, the test can evaluate the scheme only in qualitative terms. This evaluation, however, provides valuable information on the scheme's ability to simulate the fundamentals of atmospheric thermodynamics and dynamics.

The domain for this case was bounded within [0:20.0 km] × [0:10.0 km]. The mesh resolution was set to 125 m. Farfield/outflow boundary conditions were used in the lateral and the top and bottom boundaries were set as solid walls. The domain was initialized for a neutral atmosphere at $\theta_i = 300$ K in hydrostatic balance. The initial u-velocity and the v-velocity were set to zero. A potential temperature perturbation in the form of a linear function was initialized at $x_b = x_{max}/2$ and $y_b = 2000$ m:

$$\theta(x, y) = \theta_i + \Delta\theta \left(1.0 - \frac{L}{R}\right) \quad \text{if } L \leqslant R \tag{31}$$

where

$$L = \sqrt{(x - x_b)^2 + (y - y_b)^2} \tag{32}$$

The potential temperature perturbation maximum $\Delta\theta$ had a value of 2 K. The radius, R, of the perturbation was set to 2000 m. The model was run for time = 1020 s (17 min). The domain configuration is same as the one used in Wicker and Skamarock [34]—the only difference is that final time of the simulation was increased to 1020 s (17 min) from 1000 s, since the WRF output is in multiples of minute. The *monotonized-centred* (MC) limiter was used to enforce the TVD condition. The initial potential temperature field and the simulation results after time = 1020 s are shown in Figure 5 along with results from the WRF model.

The WRF set-up for this case was similar to the inertia–gravity wave case described in the previous section, except for the lateral boundary conditions (outflow boundary conditions were specified instead of periodic). The horizontal and vertical mesh resolutions for the WRF model were set to 125 m, but it should be noted that the vertical mesh resolution in metres is only an approximation. Since WRF uses a mass-based vertical coordinate system, the height of the vertical levels change with each time step. The time step in WRF simulations is a user input (rather than a calculation within the time loop) and it was set to 0.25 s. The WRF model employs an Arakawa-C staggered grid, where the geo-potential is collocated with the vertical velocity points. The geo-potential levels are used to obtain the Cartesian height. For post-processing of the data, the geo-potential and the velocity components are linearly interpolated to the mass coordinate points where the potential temperature is defined. Linear interpolation is then done to place these values on a new grid with constant height surfaces. One complication is the lowest surface on the new grid, which is 0 m in the vertical direction. This is below the lowest potential temperature surface in the WRF output files. For this test case, the value of potential temperature at height = 0 m is set to the potential temperature value at the lowest corresponding level in the WRF output.

The introduction of the thermal in the domain generates large acceleration in the centre of the bubble accompanied by downdrafts on the either side of the bubble. Since, the temperature distribution inside the bubble is linear (highest temperature at the centre) the centre of the bubble rises faster. This creates sharp gradients of temperature in the upper part of the bubble [26]. As the bubble rises, the initial symmetry of the flow field is broken and an off-axis maximum of buoyancy

DOI: 10.1002/fld

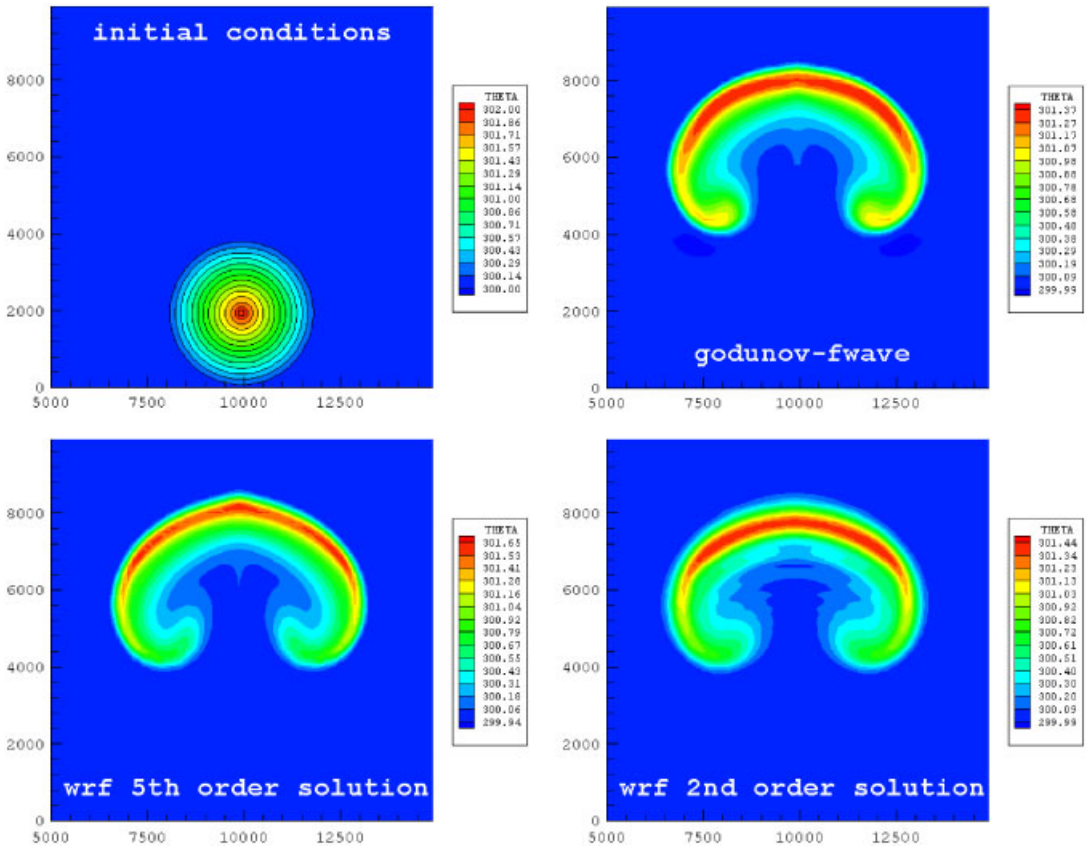

Figure 5. Convection in neutral atmosphere. Initial conditions (top-left). Godunov solution (top-right), WRF fifth-order solution (bottom-left), and WRF second-order solution at time = 1020 s (bottom-right).

is created [7]. The results can be compared with, e.g. the Wicker and Skamarock [34] solution, which exhibits spurious oscillations in the potential temperature field. These oscillations are typical of the centred finite difference schemes. The high-resolution Godunov solution presented here, on the other hand, is devoid of these oscillations. The second-order WRF scheme became unstable for this test case and a constant diffusion (with $K = 15\ \mathrm{m}^2/\mathrm{s}$) was added to stabilize the solution (shown in Figure 5). The vertical velocity acceleration and the thermal energy dissipation rates for the three models are quite similar and can be seen in the time histories plotted in Figure 6. WRF outputs data at 1 min increments and, therefore, only 17 data points were available for WRF time histories. Figure 7 shows the velocity fields obtained from the Godunov scheme after time = 1020 s into the simulation.

4.3. Modified Straka density current

The density current benchmark suggested by Straka *et al.* [36] is often used to evaluate the dynamical cores of atmospheric flow models. In this section, a modified Straka [36] benchmark is

DOI: 10.1002/fld

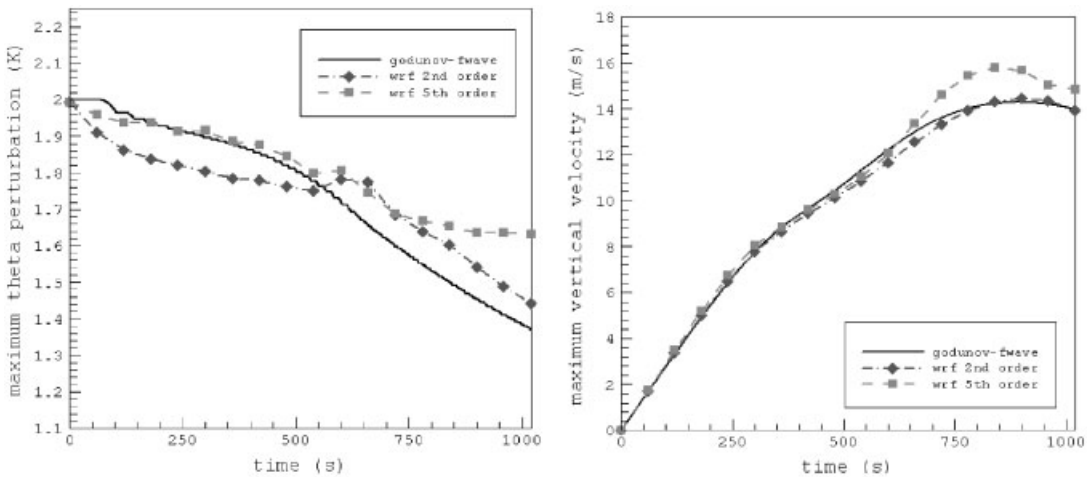

Figure 6. Convection in neutral atmosphere. Time history of domain maximum potential temperature perturbation (left) and the domain maximum vertical velocity (right) are shown in the figure.

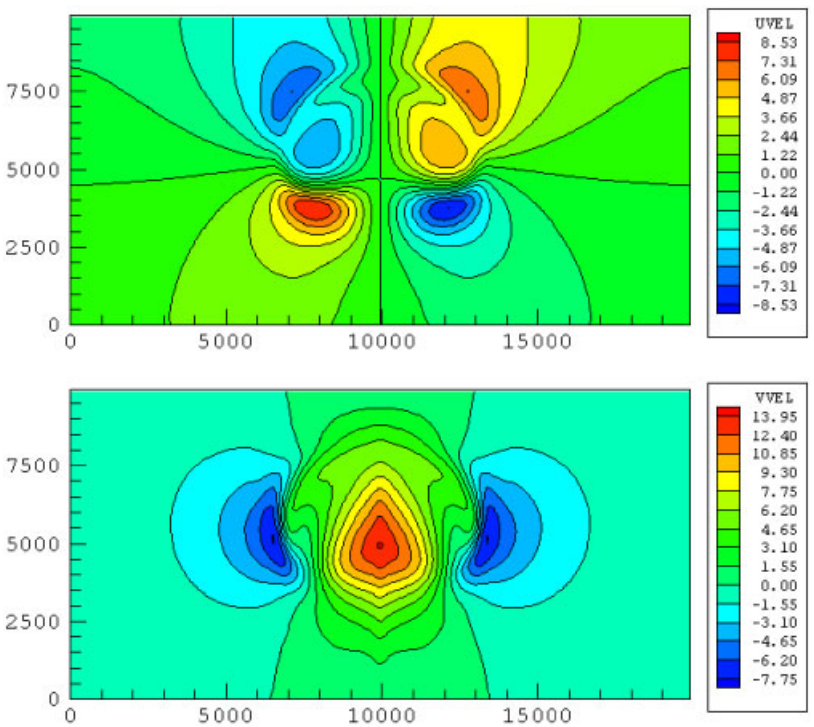

Figure 7. Convection in neutral atmosphere. u-velocity in m/s (top) and v-velocity in m/s (bottom) at simulation time = 1020 s.

DOI: 10.1002/fld

simulated with the following difference. Since only Euler solutions are considered in this study, the constant diffusion (with $K = 75\ \mathrm{m}^2/\mathrm{s}$) is not added. See Appendix B for the actual Straka benchmark.

The domain in this case was bounded within $[-26.5\ \mathrm{km}{:}26.5\ \mathrm{km}] \times [0{:}6.4\ \mathrm{km}]$. The mesh resolution was set to 50 m in both the x- and y-directions. Farfield/outflow boundary conditions were used in the lateral and the top and bottom boundaries were set as solid walls. The domain was initialized for a neutral atmosphere at 300 K in hydrostatic balance. The initial u-velocity and the v-velocity were set to zero. A cold bubble was initialized using the following relation:

$$\Delta\theta = \begin{cases} 0.0 & \text{if } L > 1.0 \\ -15.0\left[\dfrac{\cos(\pi L) + 1.0}{2}\right] & \text{if } L \leqslant 1.0 \end{cases} \tag{33}$$

where

$$L = \sqrt{\left(\frac{x - x_c}{x_r}\right)^2 + \left(\frac{y - y_c}{y_r}\right)^2} \tag{34}$$

where, $x_c = 0.0\mathrm{km}$, $y_c = 3.0\mathrm{km}$, $x_r = 4.0\mathrm{km}$ and $y_r = 2.0\mathrm{km}$. The simulation was run for 900s. The MC limiter was used to enforce the TVD condition. The potential temperature fields at different simulation times (time = 300, 600 and 900 s) are shown in Figure 8. Only the right half of the computational domain is shown in the figures.

The test case can be considered as an idealized micro-burst. As the cold air descends due to negative buoyancy, strong downdrafts develop at the centre of the cold bubble. When the cold air reaches the ground, it is rolled up and a front is formed. As this front propagates, shear is generated at the top boundary of the front. The benchmark solution [36] consists of three rotors, which develop at the top boundary of the front due to the Kelvin–Helmholtz-type instability. The formation and the propagation of the front and the development of these rotors can be seen in Figure 8. The final front location is also indicated in Figure 8, which compares well with the solutions given in Straka *et al.* [36]. The front location (in terms of potential temperature) at 14 975 m corresponds to the cell with a potential temperature value of 299.99 K—the value of potential temperature in the cell next to it (at 15 025 m) is 300.0 K. The WRF second-order simulation (not shown here) became unstable for this test case also—but the addition of explicit diffusion stabilized the solution.

4.4. Droegemeier density current

The density current benchmark suggested by Straka *et al.* [36] is based on a numerical experiment designed by Droegemeier [7, 37]. In this section, the simulation of Droegemeier's experiment is described. The domain in this case was bounded within $[0\ \mathrm{km}{:}25.0\ \mathrm{km}] \times [0{:}10.0\ \mathrm{km}]$. The mesh resolution was set to 50 m in both the x- and y-directions. Farfield/outflow boundary conditions were used in the right lateral boundary and the left lateral boundary was set to wall. The top and bottom boundaries were also set as solid walls. The domain was initialized for a neutral atmosphere at 300 K in hydrostatic balance. The initial u-velocity and the v-velocity were set to zero. A cold pool of air was initialized between $[0{:}5000\,\mathrm{m}] \times [0{:}5000\,\mathrm{m}]$, which linearly decreased

DOI: 10.1002/fld

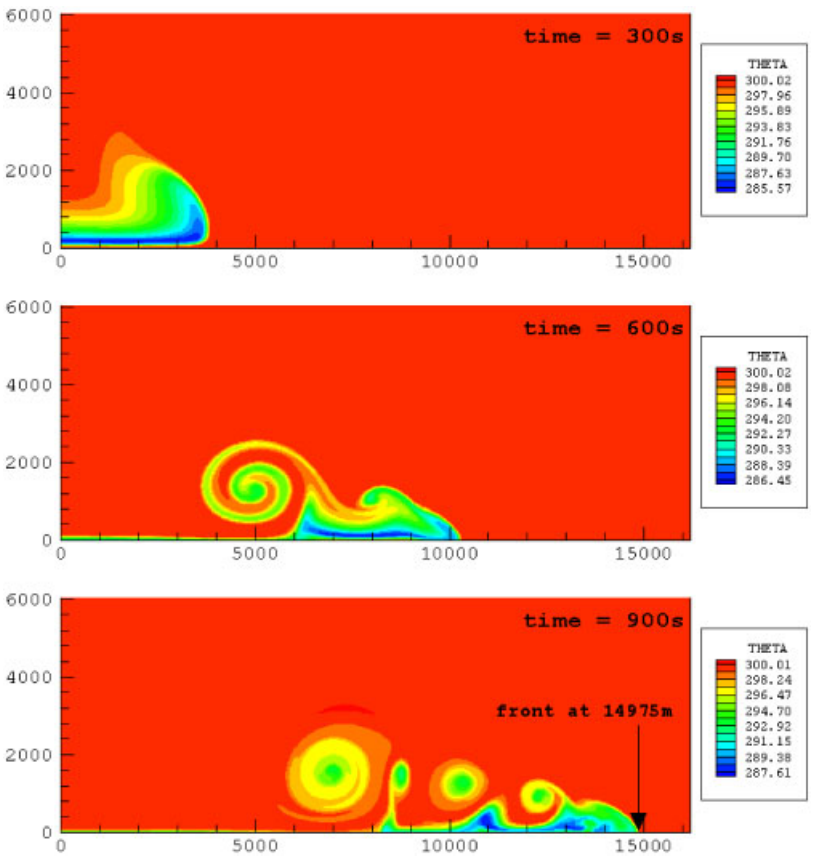

Figure 8. Density current (after Straka *et al.*). Potential temperature (K) fields at time = 300, 600, and 900 s are shown. The location of the front at time = 900 s is also given. Only a part of the right half of the computational domain is shown in the figures. The formation of a front can be seen at time = 300 s. The propagation of this front generates large amount of shear in the flow. The development of rotors due to Kelvin–Helmholtz-type instability can be seen at time = 600 and 900 s.

in temperature to 290 K at the surface (see Figure 9). The simulation was run for time = 900 s. The MC limiter was used to enforce the TVD condition.

Like in the previous density current case, the negative buoyancy sets the pool of cold air in a downward motion, and as this cold air descends, a front is formed, which propagates forward. This forward motion of the cold front generates shear at the top boundary of the front, resulting in Kelvin–Helmholtz waves. The propagation of front and the formation of these waves can be seen at time = 450 and time = 900 s into the simulation (Figure 9). Note that this is also an Euler solution and again no diffusion was added in the simulation. A qualitative comparison can be made with the solutions (PPM and centred finite difference scheme) given by Carpenter *et al.* [7].

DOI: 10.1002/fld

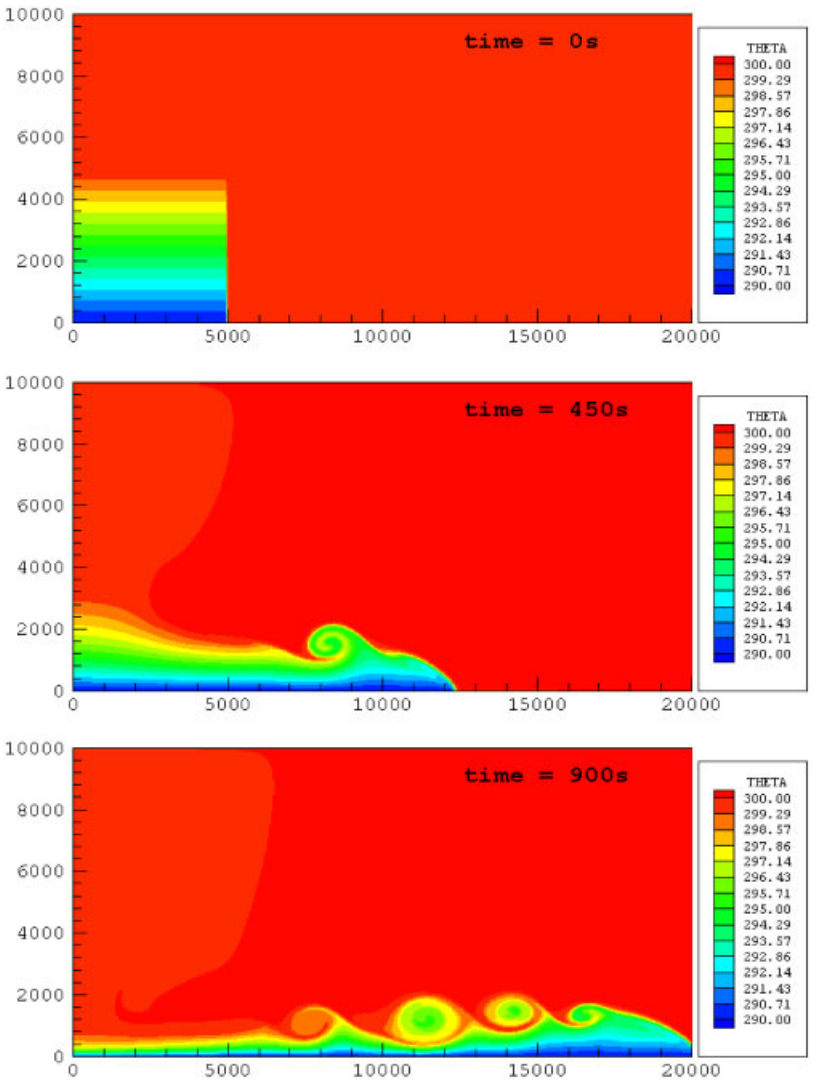

Figure 9. Density current (after Droegemeier and Wilhelmson). Potential temperature (K) fields at time = 0, 450 and 900 s are shown. The actual domain extends to 25 km in the x-direction.

5. CONCLUSIONS

A high-resolution Godunov-type scheme based on flux-based decomposition of waves after LeVeque is suggested for simulating atmospheric flow problems. Benchmark problems for the non-hydrostatic atmosphere were simulated for the validation of the scheme and the results are quite encouraging. Godunov-type high-resolution methods offer an attractive alternative for simulating atmospheric flows on the meso-, micro-, and urban-scales, which are characterized by steep gradients (micro-bursts, tornadoes, hurricanes, accidental or intentional release of hazardous

DOI: 10.1002/fld

materials in an urban area, etc.). These finite volume discretizations are conservative and have the ability to resolve regions of steep gradients accurately, thus avoiding dispersion errors in the solution. Numerical diffusion (implicit in all upwind schemes) can be overcome by higher-order extensions or using solution-adaptive methods. The positivity of scalars is also achieved by the appropriate use of limiters. A comparison with the National Center for Atmospheric Research's state-of-the-art WRF model showed that the high-resolution Godunov-type scheme performs well for flows in which sharp gradients can develop. For example, the WRF second-order scheme becomes unstable if large gradients are present in the solution (density current and convection in neutral atmosphere cases) and requires explicit filtering for stability. Although the study demonstrates the viability of using Godunov-type schemes for atmospheric flow simulations, much can be done to further improve the methodology presented here, such as inclusion of more physics (turbulence closure, surface layer physics, micro-physics, radiation transfer, etc.). The scheme can be implemented on unstructured grids and that is another avenue for future extensions.

APPENDIX A

The eigenstructure for the three-dimensional Euler equations is given in this Appendix. The homogeneous Euler equations governing atmospheric flows can be written as

$$\frac{\partial U}{\partial t}+\frac{\partial F}{\partial x}+\frac{\partial G}{\partial y}+\frac{\partial H}{\partial z}=0 \tag{A1}$$

where

$$U=\begin{bmatrix}\rho\\ \rho u\\ \rho v\\ \rho w\\ \rho\theta\end{bmatrix},\quad F=\begin{bmatrix}\rho u\\ \rho u^2+p\\ \rho uv\\ \rho uw\\ u\rho\theta\end{bmatrix},\quad G=\begin{bmatrix}\rho v\\ \rho uv\\ \rho v^2+p\\ \rho vw\\ v\rho\theta\end{bmatrix},\quad H=\begin{bmatrix}\rho w\\ \rho uw\\ \rho vw\\ \rho w^2+p\\ w\rho\theta\end{bmatrix} \tag{A2}$$

In the above relations, ρ is the density of fluid, u is the velocity component in the x-direction, v is the velocity component in the y-direction, w is the velocity component in the z-direction, p is the pressure and θ is the potential temperature. The Euler equations can be written in a quasi-linear form as

$$U_t+A(U)U_x+B(U)U_y+C(U)U_z=0 \tag{A3}$$

The subscripts t, x, y and z denote the derivatives in time and space. $A(U)$, $B(U)$ and $C(U)$ are the coefficient Jacobian matrices. The system in Equation (A3) is hyperbolic, if the matrices

DOI: 10.1002/fld

$A(U)$, $B(U)$ and $C(U)$ can be diagonalized and have real eigenvalues. $A(U)$, e.g. can be written as

$$A(U)=\begin{bmatrix} \frac{\partial f_1}{\partial u_1} & \frac{\partial f_1}{\partial u_2} & \frac{\partial f_1}{\partial u_3} & \frac{\partial f_1}{\partial u_4} & \frac{\partial f_1}{\partial u_5} \\ \frac{\partial f_2}{\partial u_1} & \frac{\partial f_2}{\partial u_2} & \frac{\partial f_2}{\partial u_3} & \frac{\partial f_2}{\partial u_4} & \frac{\partial f_2}{\partial u_5} \\ \frac{\partial f_3}{\partial u_1} & \frac{\partial f_3}{\partial u_2} & \frac{\partial f_3}{\partial u_3} & \frac{\partial f_3}{\partial u_4} & \frac{\partial f_3}{\partial u_5} \\ \frac{\partial f_4}{\partial u_1} & \frac{\partial f_4}{\partial u_2} & \frac{\partial f_4}{\partial u_3} & \frac{\partial f_4}{\partial u_4} & \frac{\partial f_4}{\partial u_5} \\ \frac{\partial f_5}{\partial u_1} & \frac{\partial f_5}{\partial u_2} & \frac{\partial f_5}{\partial u_3} & \frac{\partial f_5}{\partial u_4} & \frac{\partial f_5}{\partial u_5} \end{bmatrix} \tag{A4}$$

where

$$U=\begin{bmatrix} u_1 \\ u_2 \\ u_3 \\ u_4 \\ u_5 \end{bmatrix}=\begin{bmatrix} \rho \\ \rho u \\ \rho v \\ \rho w \\ \rho \theta \end{bmatrix} \quad \text{and} \quad F(U)=\begin{bmatrix} f_1 \\ f_2 \\ f_3 \\ f_4 \\ f_5 \end{bmatrix}=\begin{bmatrix} u_2 \\ \frac{u_2^2}{u_1}+C_0 u_5^{\gamma} \\ \frac{u_2 u_3}{u_1} \\ \frac{u_2 u_4}{u_1} \\ \frac{u_2 u_5}{u_1} \end{bmatrix} \tag{A5}$$

The elements of the matrix in Equation (A4) can be found after some algebraic manipulations, e.g.

$$\frac{\partial f_2}{\partial u_1}=\frac{\partial}{\partial u_1}\left[\frac{u_2^2}{u_1}+C_0 u_5^{\gamma}\right]=-\frac{u_2^2}{u_1^2}=\left[-\frac{\rho u \rho u}{\rho \rho}\right]=-u^2 \tag{A6}$$

$$\frac{\partial f_2}{\partial u_2}=\frac{\partial}{\partial u_2}\left[\frac{u_2^2}{u_1}+C_0 u_5^{\gamma}\right]=\frac{2u_2}{u_1}=\frac{2\rho u}{\rho}=2u \tag{A6a}$$

$$\frac{\partial f_2}{\partial u_3}=\frac{\partial}{\partial u_3}\left[\frac{u_2^2}{u_1}+C_0 u_5^{\gamma}\right]=0 \tag{A6b}$$

$$\frac{\partial f_2}{\partial u_4}=\frac{\partial}{\partial u_4}\left[\frac{u_2^2}{u_1}+C_0 u_5^{\gamma}\right]=0 \tag{A6c}$$

DOI: 10.1002/fld

$$\frac{\partial f_2}{\partial u_5} = \frac{\partial}{\partial u_5}\left[\frac{u_2^2}{u_1} + C_0 u_5^{\gamma}\right] = \gamma C_0 u_5^{\gamma-1} = \left[\frac{\gamma C_0(\rho\theta)^{\gamma}}{\rho\theta}\right] = \frac{\gamma p}{\rho\theta} = \frac{a^2}{\theta} \tag{A6d}$$

and

$$\frac{\partial f_3}{\partial u_1} = \frac{\partial}{\partial u_1}\left[\frac{u_2 u_3}{u_1}\right] = -\frac{u_2 u_3}{u_1^2} = -\frac{\rho u \rho v}{\rho\rho} = -uv \tag{A6e}$$

$$\frac{\partial f_3}{\partial u_2} = \frac{\partial}{\partial u_2}\left[\frac{u_2 u_3}{u_1}\right] = \frac{u_3}{u_1} = \frac{\rho v}{\rho} = v \tag{A6f}$$

$$\frac{\partial f_3}{\partial u_3} = \frac{\partial}{\partial u_3}\left[\frac{u_2 u_3}{u_1}\right] = \frac{u_2}{u_1} = \frac{\rho u}{\rho} = u \tag{A6g}$$

$$\frac{\partial f_3}{\partial u_4} = \frac{\partial}{\partial u_4}\left[\frac{u_2 u_3}{u_1}\right] = 0 \tag{A6h}$$

$$\frac{\partial f_3}{\partial u_5} = \frac{\partial}{\partial u_5}\left[\frac{u_2 u_3}{u_1}\right] = 0 \tag{A6i}$$

where a is the speed of sound. The remaining terms in Equation (A4) can be found in a similar manner. The matrix in Equation (A4) simplifies to

$$A(U) = \begin{bmatrix} 0 & 1 & 0 & 0 & 0 \\ -u^2 & 2u & 0 & 0 & a^2/\theta \\ -uv & v & u & 0 & 0 \\ -uw & w & 0 & u & 0 \\ -u\theta & \theta & 0 & 0 & u \end{bmatrix} \tag{A7}$$

The eigenvalues and eigenvectors corresponding to the Jacobian matrix $A(U)$ in Equation (A7) are

$$u-a: \begin{bmatrix} 1 \\ u-a \\ v \\ w \\ \theta \end{bmatrix}, \quad u: \begin{bmatrix} 1 \\ u \\ 0 \\ 0 \\ 0 \end{bmatrix}, \quad u: \begin{bmatrix} 0 \\ 0 \\ 1 \\ 0 \\ 0 \end{bmatrix}, \quad u: \begin{bmatrix} 0 \\ 0 \\ 0 \\ 1 \\ 0 \end{bmatrix}, \quad u+a: \begin{bmatrix} 1 \\ u+a \\ v \\ w \\ \theta \end{bmatrix} \tag{A8}$$

DOI: 10.1002/fld

The matrix of right eigenvectors can now be written as

$$R = \begin{bmatrix} 1 & 1 & 0 & 0 & 1 \\ u-a & u & 0 & 0 & u+a \\ v & 0 & 1 & 0 & v \\ w & 0 & 0 & 1 & w \\ \theta & 0 & 0 & 0 & \theta \end{bmatrix} \tag{A9}$$

The inverse of the matrix in Equation (A9) is given by

$$R^{-1} = \begin{bmatrix} \dfrac{u}{2a} & -\dfrac{1}{2a} & 0 & 0 & \dfrac{1}{2\theta} \\ 1 & 0 & 0 & 0 & -\dfrac{1}{\theta} \\ 0 & 0 & 1 & 0 & -\dfrac{v}{\theta} \\ 0 & 0 & 0 & 1 & -\dfrac{w}{\theta} \\ -\dfrac{u}{2a} & \dfrac{1}{2a} & 0 & 0 & \dfrac{1}{2\theta} \end{bmatrix} \tag{A10}$$

The eigenvalues and eigenvectors corresponding to $B(U)$ and $C(U)$ in Equation (A3) can be found in a similar manner. Once the complete wave structure is known, the algorithm described in this paper can be extended to the third spatial dimension.

APPENDIX B

The focus of this paper has been on the simulation of Euler equations. It is, however, also necessary to gauge the performance of the proposed scheme when the diffusion operator is included in the solution. The actual Straka non-linear density current benchmark [36] is described in this Appendix for the sake of completeness.

The domain in this case was bounded within $[-20.0\,\text{km}{:}20.0\,\text{km}] \times [0{:}6.4\,\text{km}]$. Note that the outflow boundaries in the lateral do not need to be placed too far away, since, the problem of wave reflection at the farfield boundaries is minimal for Godunov-type schemes. The mesh resolution was set to 50 m in both the x- and y-directions. Farfield/outflow boundary conditions were used in the lateral and the top and bottom boundaries were set to solid walls. The initial conditions were defined by taking the following steps:

1. The domain was initialized for a neutral atmosphere by setting the potential temperature at 300 K.
2. The initial u-velocity and the v-velocity were set to zero.

DOI: 10.1002/fld

3. The temperature profile was defined using the following relation:

$$T = 300 - \frac{yg}{c_p} \tag{B1}$$

4. Given the potential temperature field, the Exner pressure, Π, was calculated for the entire domain:

$$\frac{\partial \Pi}{\partial y} = \frac{g}{\overline{\overline{\theta}}} \tag{B2}$$

5. Pressure was calculated from the Exner pressure:

$$\Pi = \left(\frac{p}{p_0}\right)^{R_d/c_p} \tag{B3}$$

6. A cold bubble was initialized by adding a perturbation in the temperature field using the following relation:

$$\Delta T = \begin{cases} 0.0 & \text{if } L > 1.0 \\ -15.0\left[\dfrac{\cos(\pi L) + 1.0}{2}\right] & \text{if } L \leqslant 1.0 \end{cases} \tag{B4}$$

where

$$L = \sqrt{\left(\frac{x - x_c}{x_r}\right)^2 + \left(\frac{y - y_c}{y_r}\right)^2} \tag{B5}$$

where $x_c = 0.0$ km, $y_c = 3.0$ km, $x_r = 4.0$ km and $y_r = 2.0$ km. Please note that in the earlier density current simulations the perturbation was added to the potential temperature field.

7. Given the temperature field, potential temperature was re-defined for the entire domain using Equation (3).
8. Density was initialized using the gas law:

$$p = \rho R_d T \tag{B6}$$

The diffusion was added into the solution using a fractional-step method. A constant eddy viscosity/diffusivity ($K_m = K_h = K = 75$ m^2/s) was used for both the momentum and potential temperature fields. The simulation was run for time = 900 s. The potential temperature perturbation (K), u-velocity (m/s) and v-velocity (m/s) fields at time = 900 s are shown in Figure B1. The figures show a portion of the actual computational domain from approximately 0 to 16 000 m in the x-direction and 0 to 6000 m in the y-direction. The simulation results shown in Figure B1 are in good agreement with the Straka benchmark, both qualitatively and quantitatively (see Table B1). In Table B1, REFC refers to the fully compressible reference solution, REFS is the fully compressible reference solution on a staggered grid and REFQ is the reference solution using a quasi-compressible model. All reference solutions (REFC, REFS and REFQ), reported by Straka *et al.* [36], were on grids with uniform resolution of 25 m. The statistics reported in Table B1 are for the right half of the computational domain (shown in Figure B1). The location of the front for the *f-wave* solution is in terms of potential temperature and is given by the x-coordinate of the

DOI: 10.1002/fld

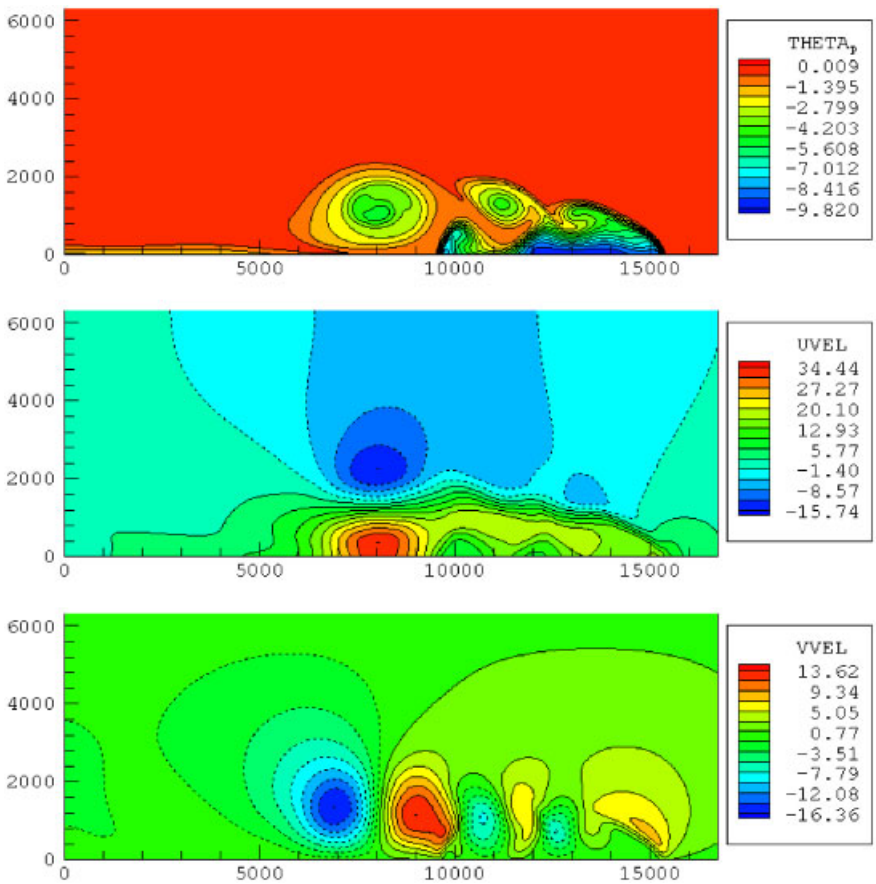

Figure B1. Non-linear density current benchmark; potential temperature perturbation (K)—top, u-velocity (m/s)—middle, and v-velocity (m/s)—bottom. Time = 900 s. Dashed lines indicate negative values.

Table B1. Comparison of the *f-wave*-Godunov results with the Straka density current benchmarks.

Variable	*f-wave*	REFC	REFS	REFQ
$p'_{\max}$ (mb)	1.26	2.87	2.49	1.74
$p'_{\min}$ (mb)	−6.27	−5.14	−5.55	−5.21
$\theta'_{\max}$ (K)	8.92E−03	0.00	0.00	0.00
$\theta_{\min}$(K)	−9.82	−9.77	−9.77	−10.00
$u_{\max}$ (m/s)	34.44	36.46	35.02	34.72
$u_{\min}$ (m/s)	−15.74	−15.19	−16.32	−15.31
$v_{\max}$ (m/s)	13.62	12.93	13.28	13.04
$v_{\min}$ (m/s)	−16.36	−15.95	−16.11	−16.89
Front location (m)	15 525.00	15 537.44	N/A	15 509.17

DOI: 10.1002/fld

cell in the lowest level with a potential temperature of 299.99 K. The Godunov-*f-wave* solution also compares well with other reported solutions of the benchmark (e.g. see [38, 39]).

ACKNOWLEDGEMENTS

Many thanks to Prof. Randall J. LeVeque for providing the CLAWPACK version, which implements the *f-waves* decomposition for solving the Riemann problem. This software was used as a template for implementing the Riemann solver for conservation laws governing atmospheric flows. We are grateful to Dr R. J. Purser for reviewing the paper and for his helpful comments.

REFERENCES

1. Godunov SK. A finite difference method for the computation of discontinuous solutions of the equations of fluid dynamics. *Matematicheskii Sbornik* 1959; **47**:357–393.
2. Van Leer B. Towards the ultimate conservative difference scheme V. A second-order sequel to Godunov's method. *Journal of Computational Physics* 1979; **32**:101–136.
3. Van Leer B. An introduction to the article 'Reminiscences about Difference Schemes' by S. K. Godunov. *Journal of Computational Physics* 1999; **153**:1–5.
4. Ahmad N, Boybeyi Z, Löhner R, Sarma A. A Godunov-type finite volume scheme for flows on meso- and micro-scales. *AIAA Paper 2005-1234*.
5. Toro EF, Spruce M, Speares W. Restoration of the contact surface in the HLL Riemann solver. *Shock Waves* 1994; **4**:25–34.
6. Botta N, Klein R, Langenberg S, Lutzenkirchen S. Well balanced finite volume methods for nearly hydrostatic flows. *Journal of Computational Physics* 2004; **196**:539–565.
7. Carpenter RL, Droegemeier KK, Woodward PR, Hane CE. Application of the piecewise parabolic method (PPM) to meteorological modeling. *Monthly Weather Review* 1990; **118**:586–612.
8. Colella P, Woodward PR. The piecewise parabolic method (PPM) for gas-dynamical simulations. *Journal of Computational Physics* 1984; **54**:174–201.
9. Smolarkiewicz PK. A fully multidimensional positive definite advection transport algorithm with small implicit diffusion. *Journal of Computational Physics* 1984; **54**:325–362.
10. Brooks HE, Doswell III CA. Extreme winds in high-precipitation supercells. *Preprints of the 17th Conference On Severe Local Storms*, Saint Louis, Missouri, 1993; 173–177.
11. Shaw BL, Pielke RA, Ziegler CL. A three-dimensional numerical simulation of a great plains dryline. *Monthly Weather Review* 1997; **125**:1489–1506.
12. Gopalakrishnan SG, Bacon D, Ahmad N, Boybeyi Z, Dunn T, Jin Y, Hall M, Lee P, Mays D, Sarma A, Turner M, Wait T. An operational multiscale hurricane forecasting system. *Monthly Weather Review* 2002; **130**:1830–1847.
13. Durran DR. The third-order Adams–Bashforth method: an attractive alternative to leapfrog time differencing. *Monthly Weather Review* 1991; **119**:702–720.
14. Mendez-Nuñez LR, Carroll JJ. Comparison of Leapfrog, Smolarkiewicz and MacCormack schemes applied to nonlinear equations. *Monthly Weather Review* 1993; **121**:565–578.
15. Bott A. A positive definite advection scheme obtained by non-linear renormalization of the advective fluxes. *Monthly Weather Review* 1989; **117**:1006–1015.
16. Boris J, Book DL. Flux-corrected transport. I. SHASTA, a fluid transport algorithm that works. *Journal of Computational Physics* 1973; **11**:38–69.
17. Zalesak ST. Fully multidimensional flux-corrected transport algorithms for fluids. *Journal of Computational Physics* 1979; **31**:335–362.
18. Klemp JB, Skamarock WC, Dudhia J. Conservative split–explicit time integration methods for the compressible nonhydrostatic equations. *WRF Eulerian Prototype Model Equations Draft Manuscript*, National Center for Atmospheric Research, 2000.
19. Bacon DP, Ahmad NN, Boybeyi Z, Dunn TJ, Hall MS, Lee PCS, Sarma RA, Turner MD, Waight K, Young S, Zack J. A dynamically adapting weather and dispersion model: the operational multiscale environment model with grid adaptivity (OMEGA). *Monthly Weather Review* 2000; **128**:2044–2076.
20. Smolarkiewicz PK. Multidimensional positive definite advection transport algorithm: an overview. *International Journal for Numerical Methods in Fluids* 2006; **50**(10):1123–1144.

DOI: 10.1002/fld

21. Ahmad N, Bacon D, Hall M, Sarma A. Application of the multi-dimensional positive definite advection transport algorithm (MPDATA) to environmental modeling on adaptive unstructured grids. *International Journal for Numerical Methods in Fluids* 2006; **50**(10):1247–1268.
22. LeVeque RJ. *Finite Volume Methods for Hyperbolic Problems*. Cambridge University Press: Cambridge, MA, 2002.
23. Bale D, LeVeque RJ, Mitran S, Rossmanith JA. A wave-propagation method for conservation laws and balance laws with spatially varying flux functions. *SIAM Journal on Scientific Computing* 2002; **24**:955–978.
24. Roe PL. Approximate Riemann solvers, parameter vectors, and difference schemes. *Journal of Computational Physics* 1981; **43**:357–372.
25. Ooyama KV. A thermodynamic foundation for modelling the moist atmosphere. *Journal of Atmospheric Science* 1990; **47**:2580–2593.
26. Korain D, Isakov V, Mendez-Nuñez L. A cloud-resolving model with the radiation scheme based on the Monte Carlo method. *Atmospheric Research* 1998; **47**:437–459.
27. LeVeque RJ. High-resolution conservative algorithms for advection in incompressible flow. *SIAM Journal on Numerical Analysis* 1996; **33**:627–665.
28. LeVeque RJ. Wave propagation algorithms for multi-dimensional hyperbolic systems. *Journal of Computational Physics* 1997; **131**:327–353.
29. LeVeque RJ. *Conservation Law Package* (*CLAWPACK*) *Version 4.2—User's Guide*'. University of Washington, 2003.
30. Brio M, Zakharian AR, Webb GM. Two-dimensional Riemann solver for Euler equations of gas dynamics. *Journal of Computational Physics* 2001; **167**:177–195.
31. Langseth JO, LeVeque RJ. A wave-propagation method for three-dimensional hyperbolic conservation laws. *Journal of Computational Physics* 2000; **165**:126–166.
32. Skamarock WC, Klemp JB. Efficiency and accuracy of the Klemp–Wilhelmson time-splitting technique. *Monthly Weather Review* 1994; **122**:2623–2630.
33. Jameson A, Schmidt W, Turkel E. Numerical solution of the Euler equations by finite volume method using Runge–Kutta time stepping schemes. *AIAA Paper 1981-1259*.
34. Wicker LJ, Skamarock WC. A time-splitting scheme for the elastic equations incorporating second-order Runge–Kutta time differencing. *Monthly Weather Review* 1998; **126**:1992–1999.
35. Mendez-Nuñez LR, Carroll JJ. Application of the MacCormack scheme to atmospheric nonhydrostatic models. *Monthly Weather Review* 1994; **122**:984–1000.
36. Straka JM, Wilhelmson RB, Wicker LJ, Anderson JR, Droegemeier KK. Numerical solutions of a non-linear density current: a benchmark solution and comparisons. *International Journal for Numerical Methods in Fluids* 1993; **17**:1–22.
37. Droegemeier KK, Wilhelmson RB. Numerical simulations of thunderstorm outflow dynamics. Part I: Outflow sensitivity experiments and turbulence dynamics. *Journal of Atmospheric Science* 1987; **44**:1180–1210.
38. Janjic ZI, Gerrity JP, Nickovic S. An alternative approach to nonhydrostatic modeling. *Monthly Weather Review* 2001; **129**:1164–1178.
39. Xue M, Droegemeier KK, Wong V. The advanced regional prediction system (ARPS)—a multi-scale nonhydrostatic atmospheric simulation and prediction model. Part I: Model dynamics and verification. *Meteorology and Atmospheric Physics* 2000; **75**:161–193.

DOI: 10.1002/fld